Article

Enhanced Photo-Fenton Activity of SnO$_2$/α-Fe$_2$O$_3$ Composites Prepared by a Two-Step Solvothermal Method

Pinghua Li [1], Xuye Zhuang [1,2,*], Jiahuan Xu [3], Liuxia Ruan [4], Yangfan Jiang [4], Jiaxin Lin [4] and Xianmin Zhang [4,*]

[1] School of Mechanical Engineering, Shandong University of Technology, Zibo 255049, China; lipinghua@sdut.edu.cn
[2] State Key Laboratory of Applied Optics, Changchun Institute of Optics, Fine Mechanics and Physics, Chinese Academy of Sciences, Changchun 130033, China
[3] School of Science, Jiangsu University of Science and Technology, Zhenjiang 212100, China; jiahuanxu@just.edu.cn
[4] School of Material Science and Engineering, Northeastern University, Shenyang 110819, China; 1710168@stu.neu.edu.cn (L.R.); 1870323@stu.neu.edu.cn (Y.J.); 1800508@stu.neu.edu.cn (J.L.)
* Correspondence: zxye@sdut.edu.cn (X.Z.); zhangxm@atm.neu.edu.cn (X.Z.)

Abstract: The x-SnO$_2$/α-Fe$_2$O$_3$ (x = 0.04, 0.07, and 0.1) heterogeneous composites were successfully prepared via a two-step solvothermal method. These composites were systematically characterized by the X-ray diffraction technique, field emission scanning electron microscopy, an energy dispersive spectrometer, X-ray photoelectron spectroscopy and a UV–visible spectrometer. It was found that SnO$_2$ nanoparticles were uniformly decorated on the surface of α-Fe$_2$O$_3$ particles in these heterogeneous composites. A comparative study of methylene blue (MB) photodegradation by α-Fe$_2$O$_3$ and x-SnO$_2$/α-Fe$_2$O$_3$ composites was carried out. All x-SnO$_2$/α-Fe$_2$O$_3$ composites showed higher MB photodegradation efficiency than α-Fe$_2$O$_3$. When x = 0.07, the MB photodegradation efficiency can reach 97% in 60 min. Meanwhile, the first-order kinetic studies demonstrated that the optimal rate constant of 0.07-SnO$_2$/α-Fe$_2$O$_3$ composite was 0.0537 min^{-1}, while that of pure α-Fe$_2$O$_3$ was only 0.0191 min^{-1}. The catalytic mechanism of MB photodegradation by SnO$_2$/α-Fe$_2$O$_3$ was examined. The SnO$_2$ can act as a sink and help the effective transfer of photo-generated electrons for decomposing hydrogen peroxide (H$_2$O$_2$) into active radicals. This work can provide a new insight into the catalytic mechanism of the photo-Fenton process.

Keywords: hydrothermal method; heterogeneous composite; morphology; photo-Fenton activity; photodegradation

1. Introduction

As an important advanced oxidation process, the heterogeneous photo-Fenton system has been considered a promising method for the removal of stubborn organic dyes [1–4]. In this process, iron-based catalysts are generally applied to activate H$_2$O$_2$ in order to generate strong oxidative hydroxyl radicals (·OH) [5–8]. Among the iron-based catalysts, α-Fe$_2$O$_3$ is one of the most promising Fenton candidates due to its stable structure, low cost, wide absorption of visible light, and environmental benignity [9,10]. However, several adverse factors seriously reduce the reaction activity of α-Fe$_2$O$_3$, such as the high recombination rate of photoelectrons and holes, and a weak activation in alkaline environments. To remedy these drawbacks, various measures have been studied, such as porous regulation [11–16], facet engineering [17–20], and composite construction [21–26]. Among these methods, integrating α-Fe$_2$O$_3$ with other catalysts has caught the attention of many because it can effectively separate photo-generated electron–hole pairs. Liu et al. [27] reported the synthesis of α-Fe$_2$O$_3$ anchored to a graphene oxide nanosheet. The graphene oxide was considered to accelerate the transfer of photo-generated electrons and to enhance the absorption to methylene blue (MB) through electro-static interaction and π–π stacking.

Deng et al. [28] constructed an advanced $TiO_2/Fe_2TiO_5/Fe_2O_3$ heterojunction structure, and the abundant phase interfaces improved both the migration and separation of charges.

SnO_2 has a high photochemical property and stability, and is extensively studied in the fields of Li-ion batteries [29–31], dye sensitized solar cells [32–34], and gas sensors [35–37]. Additionally, many studies have shown that the SnO_2/α-Fe_2O_3 heterogeneous catalyst has an excellent photodegradation activity. Wang et al. [38] synthesized SnO_2-encapsulated α-Fe_2O_3 nanocubes by annealing Prussian blue microcubes, and revealed the important contribution of SnO_2 cubic shells for improving photocatalytic performance. Tian et al. [39] prepared a tube-like SnO_2/α-Fe_2O_3 heterostructure by using an anion-assisted hydrothermal route and studied the effective separation of photo-generated carriers. Niu et al. [40] synthesized branched SnO_2/α-Fe_2O_3 composites by a hydrothermal system of $Sn(OH)_6^{2-}$ dilute aqueous solution, and investigated their photocatalytic activity. The synthesis methods can significantly influence the morphology of SnO_2/α-Fe_2O_3 composites. First, the SnO_2 and α-Fe_2O_3 were prepared by a sol–gel method, then their composite (SnO_2–α-Fe_2O_3) systems were synthesized by combining SnO_2 with α-Fe_2O_3 in various weight percent ratios, and finally, the photocatalytic activity was investigated [41]. A necklace-like SnO_2/α-Fe_2O_3 hierarchical heterostructure was fabricated by the chemical vapor deposition method, using SnO_2 nanowires with the preferential growth direction of [1] as a template, and then the photocatalytic property was studied [42]. Therefore, it is interesting to explore the new synthesis methods as well as establish the relationship between morphology and internal catalytic mechanism of SnO_2/α-Fe_2O_3 composites.

In this study, we synthesized the x-SnO_2/α-Fe_2O_3 (x = 0.04, 0.07, and 0.1) heterogeneous catalysts via a two-step hydrothermal method. The materials were systematically characterized by using the X-ray diffraction (XRD) technique, field emission scanning electron microscopy (FE-SEM), X-ray photoelectron spectroscopy (XPS), and a UV–visible (UV–vis) spectrometer. The XRD analysis indicated the successful synthesis of purity and well-crystalline of SnO_2/α-Fe_2O_3 powders. FE-SEM images showed that SnO_2 nanoparticles were homogeneously decorated on the surface of the peach-like α-Fe_2O_3. XPS measurement demonstrated Fe and Sn elements in the 0.07-SnO_2/α-Fe_2O_3 sample to be trivalent and tetravalent, respectively. The UV–vis spectra revealed the strong visible light absorption ability of SnO_2/α-Fe_2O_3 powders. The photodegradation of MB over different catalysts was tested, and the first-order kinetic analysis was performed to get the photodegradation rate. Free radical trapping experiments and hydroxyl radical quantitative experiments were carried out to explore the mechanism of photocatalytic reaction.

2. Experimental Section

2.1. Materials and Chemicals

Ferric chloride hexahydrate ($FeCl_3 \cdot 6H_2O$) (Macklin, Shanghai, China), tin chloride pentahydrate ($SnCl_4 \cdot 5H_2O$) (Macklin, Shanghai, China), urea ($CO(NH_2)_2$) (Macklin, Shanghai, China), polyethylene glycol (PEG) (Sinopharm, Shanghai, China), sodium hydroxide (NaOH) (Sinopharm, Shanghai, China), ethanol (C_2H_5OH) (Sinopharm, Shanghai, China), and methylene blue (MB) (Sinopharm, Shanghai, China) were used in the experiment. All the reagents were analytical grade and used as received without further purification. Deionized water was used throughout the experiment.

2.2. Synthesis

2.2.1. Synthesis of α-Fe_2O_3

The peach-like α-Fe_2O_3 powders were prepared by a facile hydrothermal method, as shown in the upper section of Scheme 1. First, 1.623 g of $FeCl_3 \cdot 6H_2O$, 0.6 g of polyethylene glycol, and 0.6 g of NaOH were dissolved in 60 mL of deionized water. Secondly, the mixture solution was stirred for 30 min and transferred into a 100 mL Teflon-lined stainless steel autoclave (H-100ml, Zhuoran Company, Zhengzhou, China). The thermal treatment was performed at 180 °C for 5 h. After the autoclave was naturally cooled down to room

temperature, the precipitate was continually washed with deionized water and absolute ethanol. Finally, the α-Fe$_2$O$_3$ was achieved after being dried out at 60 °C for 2 h.

Scheme 1. Schematic diagram of the two-step synthesis process.

2.2.2. Synthesis of SnO$_2$/α-Fe$_2$O$_3$

The SnO$_2$/α-Fe$_2$O$_3$ composites were prepared via a two-step hydrothermal method. In this method, the first step is used to prepare α-Fe$_2$O$_3$ precursors as in the above description. The second step is to grow SnO$_2$ on the surface of α-Fe$_2$O$_3$ precursors as follows (shown in the bottom of Scheme 1). The x g (x = 0.04, 0.07, and 0.1, which denoted the mass of tin chloride pentahydrate) SnCl$_4$·5H$_2$O, 0.5 g of CO(NH$_2$)$_2$ were dispersed in a mixed solvent consisting of 30 mL of deionized water and 20 mL of absolute ethanol. Then, 0.1 g of the α-Fe$_2$O$_3$ precursor was added into the above solution. Subsequently, the mixture solution was stirred for 10 min before transferred into a 100 mL Teflon-lined stainless steel autoclave. The autoclave was sealed and heated at 170 °C for 10 h and then naturally cooled down to room temperature. The obtained SnO$_2$/α-Fe$_2$O$_3$ photocatalysts were washed several times with deionized water and absolute ethanol before they were dried at 60 °C for 12 h. The final products were termed as x-SnO$_2$/α-Fe$_2$O$_3$ (x = 0.04, 0.07, and 0.1). The precise control of reaction temperatures is very important to obtain target samples with good crystal structures and homogeneous particle size [43]. Pure SnO$_2$ can also be obtained by the process in the bottom of Scheme 1 without adding the α-Fe$_2$O$_3$.

2.3. Characterization

Phase structures of powders were analyzed by XRD using Japan Rigaku (Tokyo, Japan) with a Cu target. The morphologies and chemical compositions of samples were characterized by FE-SEM (JEM-7001F, JEOL, Tokyo, Japan), equipped with an energy dispersive spectroscope (EDS). X-ray photoelectron spectroscopy of SnO$_2$/α-Fe$_2$O$_3$ was detected using Thermo Fisher 250-XI (Thermofisher, Waltham, MA, USA) with an Al Kα. The optical properties and photocatalytic activities were measured using a UV–vis spectrophotometer (Shanghai Metash, UV-9000S, Shanghai, China). The molar ratios of composites were checked by an inductive coupled plasma emission spectrometer (Agilent ICP-MS 7500a, Santa Clara, CA, USA).

2.4. Photodegradation Experiment

The photo-Fenton activity of the samples was investigated by the degradation of MB dyes under visible light irradiation. The light source used was a 300 W xenon lamp with a 420 nm cutoff filter (Microsolar 300, PerfectLight, Beijing, China). In a typical procedure, 20 mg of as-prepared samples was dispersed into 100 mL of MB solution (20 mg·L^{-1}) with the assistance of ultrasonic for 2 min. Afterwards, the reaction mixture was magnetically stirred in the dark for 30 min to ensure absorption equilibrium. The reaction was initiated by adding 1 mL hydrogen peroxide solution (H_2O_2, 30 wt%, Sinopharm, Shanghai, China) after the xenon light was stable. During the irradiation, 4 mL solution was sampled at 10 min intervals. The whole process took place under stirring, while the circulating cooling water worked at the same time. After removing the catalysts from each sample by centrifugation, the degree of photodegradation was calculated by measuring the absorbance of MB at 664 nm where the solution had the maximum absorption.

3. Results and Discussion

The crystal structure of as-prepared α-Fe$_2$O$_3$ precursors, SnO$_2$, and x-SnO$_2$/α-Fe$_2$O$_3$ (x = 0.04, 0.07, and 0.1) powders were measured by XRD. As shown in Figure 1, all the peaks appearing in the α-Fe$_2$O$_3$ powders are sharp and well indexed to a pure rhombohedral structure of hematite (JCPDS No. 33-0664). This indicates the high purity and good crystallinity of the prepared α-Fe$_2$O$_3$ sample. The widths of peaks of SnO$_2$ are much larger than that of α-Fe$_2$O$_3$, which might be attributed to the poor crystallinity and small particle size of SnO$_2$. After being decorated by SnO$_2$, all the extra diffraction peaks of x-SnO$_2$/α-Fe$_2$O$_3$ were indexed to (110), (101), and (211) planes of rutile phase of SnO$_2$ (JCPDS No. 41-1445). This illustrates the successful synthesis of x-SnO$_2$/α-Fe$_2$O$_3$ composites. The particle size was estimated using the Scherrer equation [44]: $D = \frac{K\lambda}{\beta \cos\theta}$ where D is the grain size, K is the Scherrer's constant, λ is the X-ray wavelength (0.154 nm), β is the FHWM, and θ is the diffraction angle. The grain sizes of SnO$_2$, α-Fe$_2$O$_3$, and 0.07-SnO$_2$/α-Fe$_2$O$_3$ are about 15 nm, 203 nm, and 212 nm, respectively.
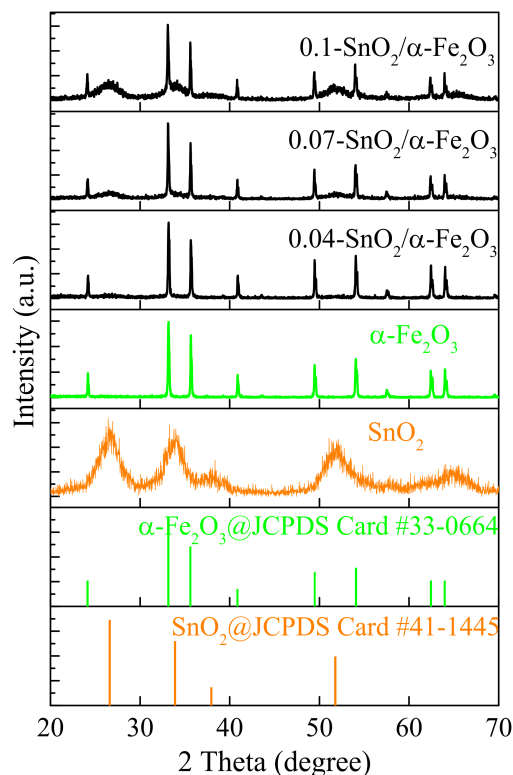
Figure 1. XRD patterns of α-Fe$_2$O$_3$, SnO$_2$, and x-SnO$_2$/α-Fe$_2$O$_3$ (x = 0.04, 0.07, and 0.1) powders.

The morphologies of α-Fe$_2$O$_3$ and 0.07-SnO$_2$/α-Fe$_2$O$_3$ were measured by FE-SEM. As shown in Figure 2a, α-Fe$_2$O$_3$ is peach-like, and the inwardly concave symmetry curve can be clearly observed on the surface of α-Fe$_2$O$_3$. The α-Fe$_2$O$_3$ particle is homogeneous, with a diameter of around 220 nm. Interestingly, many small spots are decorated on the outer surface of α-Fe$_2$O$_3$ after adding Sn, as shown in Figure 2b. Moreover, those spots, each of around 20 nm, are uniformly distributed. The particle sizes essentially agree with the results from the above XRD, which were calculated using the Scherrer's equation. Figure 2c indicates the EDS spectra of 0.07-SnO$_2$/α-Fe$_2$O$_3$. It clearly identifies that the composite is composed of Fe, O, and Sn elements. Considering the XRD of 0.07-SnO$_2$/α-Fe$_2$O$_3$, it is reasonable to assume that these small spots are SnO$_2$. The chemical compositions of x-SnO$_2$/α-Fe$_2$O$_3$ (x = 0.04, 0.07, and 0.1) were checked by ICP-MS. The mass contents of Fe$_2$O$_3$ and SnO$_2$ in 0.04-SnO$_2$/α-Fe$_2$O$_3$, 0.07-SnO$_2$/α-Fe$_2$O$_3$, and 0.1-SnO$_2$/α-Fe$_2$O$_3$ are 87.3% and 12.7%, 78.5% and 21.5%, and 70.6% and 29.4%, respectively.
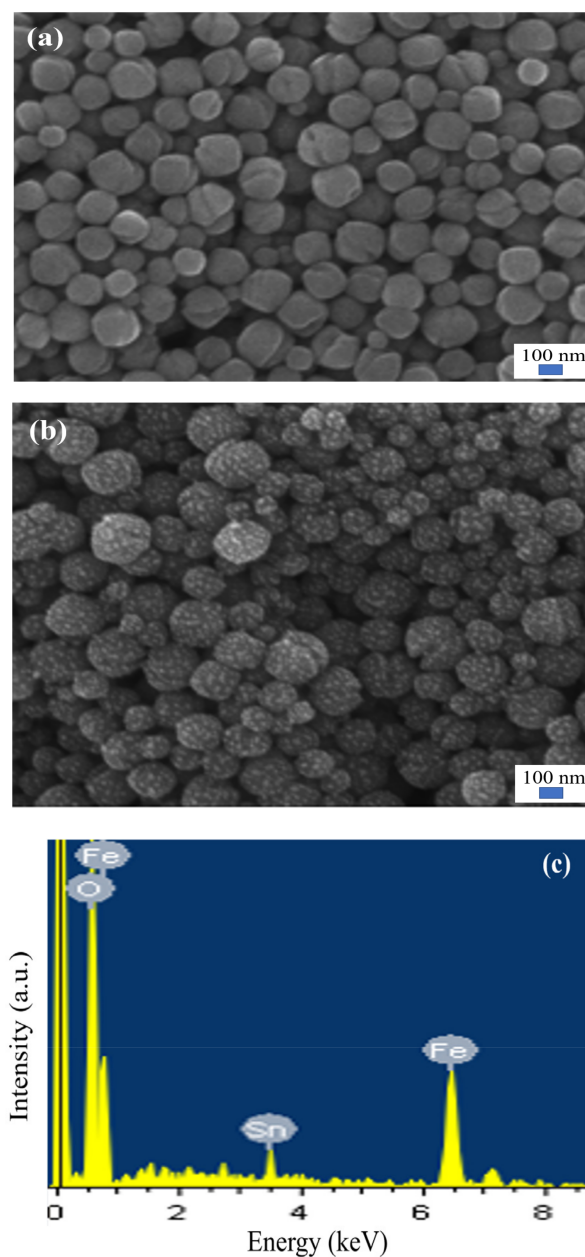
Figure 2. FE-SEM images of (**a**) α-Fe$_2$O$_3$, (**b**) 0.07-SnO$_2$/α-Fe$_2$O$_3$ and (**c**) EDS spectra of 0.07-SnO$_2$/α-Fe$_2$O$_3$.

To further demonstrate the compositions of surface dots and the oxidation states of metal elements of 0.07-SnO$_2$/α-Fe$_2$O$_3$ powders, an XPS measurement was taken. Figure 3a shows the full-scale XPS spectrum, and the presence of Sn, Fe, O, and C was confirmed without any other element. The characteristic peak of C 1s found at 284.8 eV was from adventitious carbon. Figure 3b is the high-resolution XPS spectrum of Fe 2p. The binding energy peaks at both 710.5 and 724.5 eV were ascribed to Fe 2p$_{3/2}$ and Fe 2p$_{1/2}$, respectively. The peak for Fe 2p$_{3/2}$ at 710.5 eV is sharper than that for Fe 2p$_{1/2}$ due to the spin–orbit coupling [45]. The appearance of satellite peaks at 712.8 and 733.5 eV confirms that the Fe element in 0.07-SnO$_2$/α-Fe$_2$O$_3$ is trivalent. A high intensity peak at the binding energy of 716.6 eV is due to the presence of Sn 3p$_{3/2}$. Figure 3c shows the high-resolution XPS spectrum of Sn 3d. The peaks at 487.2 and 495.5 eV were attributed to Sn 3d$_{5/2}$ and Sn 3d$_{3/2}$, respectively. This could support the +4 oxidation states of SnO$_2$. Thus, the results clearly confirm that these heterogeneous catalysts are composed of 0.07-SnO$_2$/α-Fe$_2$O$_3$, agreeing with the XRD results in Figure 1.
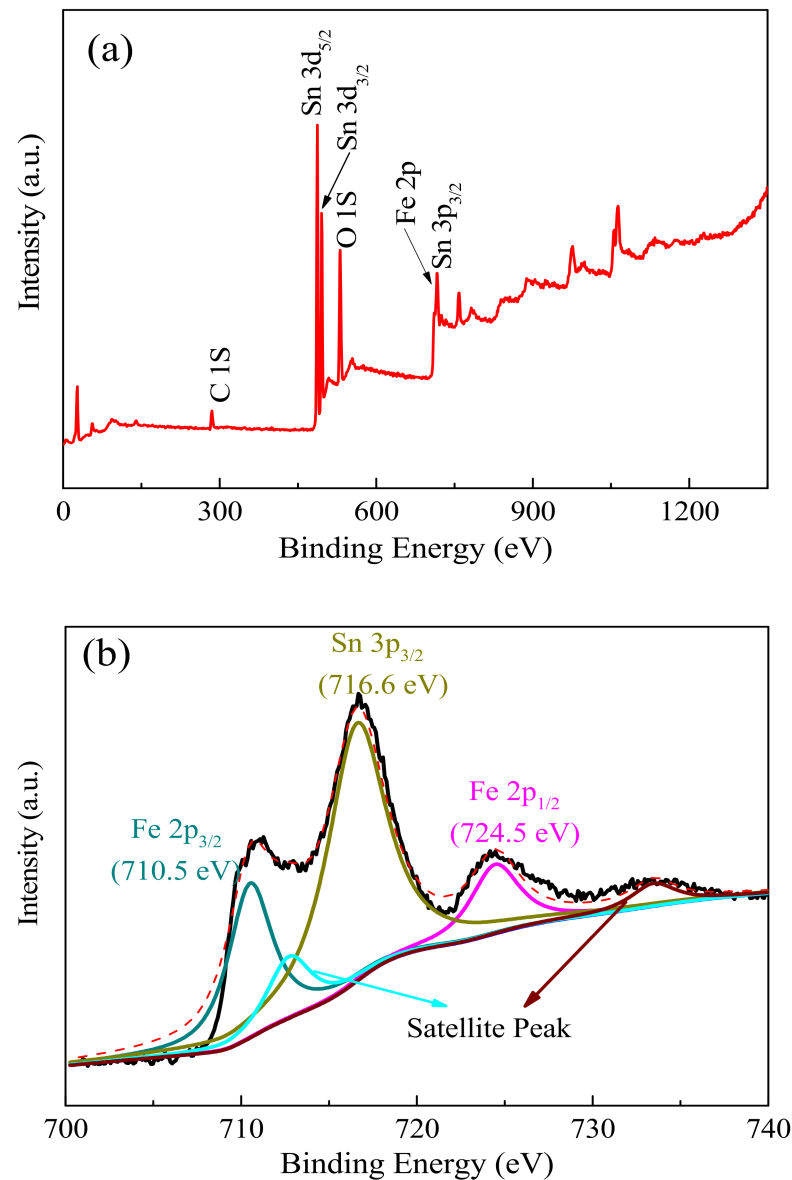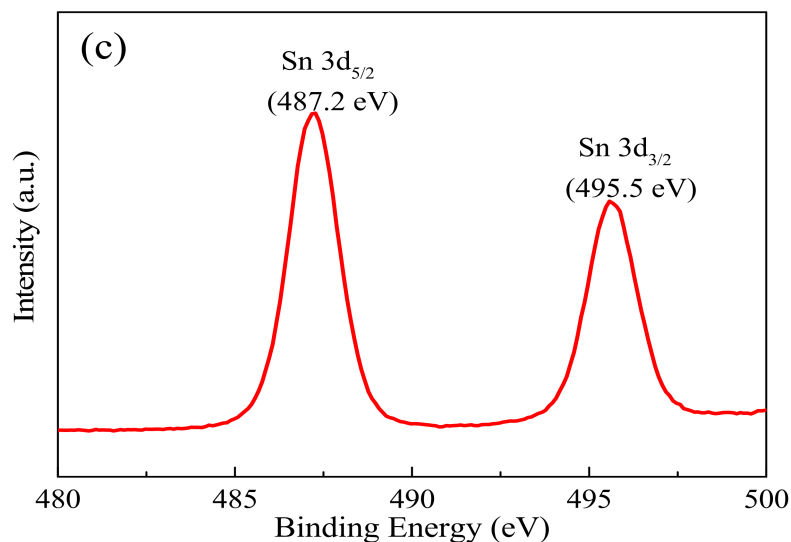

Figure 3. *Cont.*

Figure 3. XPS spectra of as-synthesized 0.07-SnO_2/α-Fe_2O_3 photocatalyst. (**a**) The survey spectrum. The high-energy resolution spectra of (**b**) Fe 2p and (**c**) Sn 3d.

In order to study the visible light absorption properties of α-Fe_2O_3, SnO_2, and 0.07-SnO_2/α-Fe_2O_3 samples, their UV–vis absorption spectra were measured, as shown in Figure 4. The present SnO_2 could hardly absorb visible light (λ > 420 nm) in the UV–vis diffuse reflection spectrum, agreeing with the literature [46,47]. Interestingly, the 0.07-SnO_2/α-Fe_2O_3 composite exhibited much higher photo absorption ability compared with pure α-Fe_2O_3. This might contribute to the improvements in the photocatalytic activities of 0.07-SnO_2/α-Fe_2O_3.
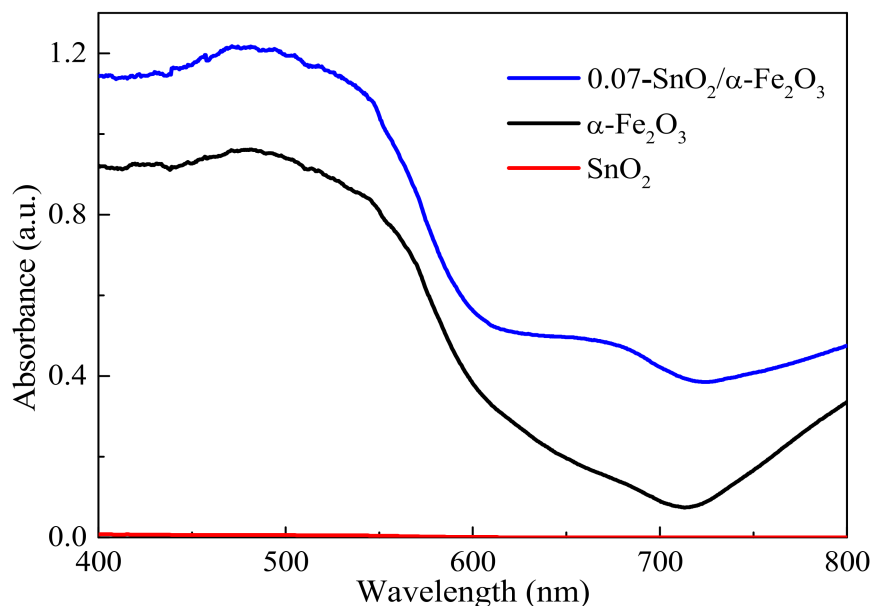

Figure 4. UV–vis spectra of α-Fe_2O_3, SnO_2, and 0.07-SnO_2/α-Fe_2O_3 samples.

The photo-Fenton activities of the present samples were studied using a degrading MB experiment under visible light for 60 min. One milliliter of H_2O_2 was added to the MB solution to activate the Fenton reaction. Figure 5a shows the visible light Fenton degradation of MB under different catalysts, including α-Fe_2O_3, SnO_2, and x-SnO_2/α-Fe_2O_3 (x = 0.04, 0.07, and 0.1) heterogeneous catalysts. Self-degradation of MB is limited. In the dark stage, SnO_2 shows excellent adsorption of dye molecules, while α-Fe_2O_3

presents poor adsorption. The adsorption capacity of the x-SnO_2/α-Fe_2O_3 composite was improved due to the decoration of SnO_2. More adsorption means a closer contact between the catalyst and the dye molecules, which might contribute to the photo-Fenton reaction. Under visible light irradiation, 66% of the MB was degraded within 60 min in the presence of α-Fe_2O_3. Interestingly, the MB degradation of x-SnO_2/α-Fe_2O_3 was much faster than that of α-Fe_2O_3. Moreover, with the increase in SnO_2 dosage, the degradation efficiency increased and then decreased, reaching the optimal efficiency of 97% for the 0.07-SnO_2/α-Fe_2O_3 sample.
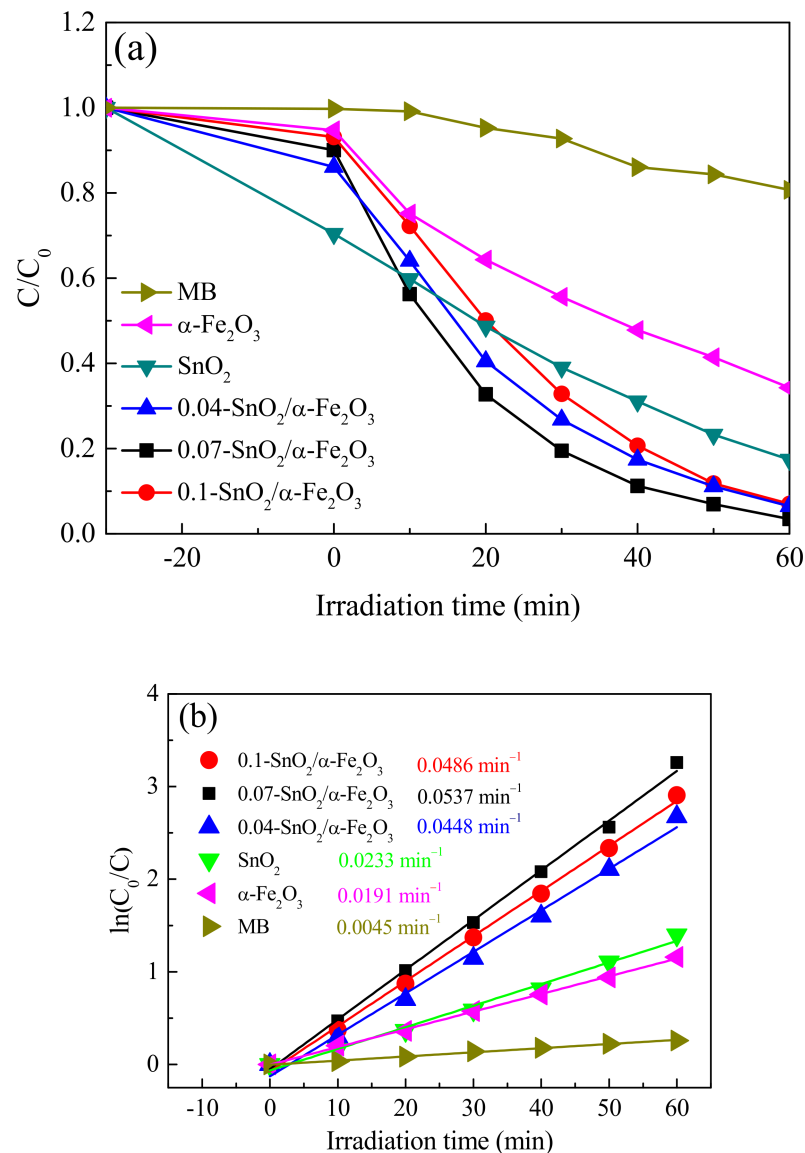

Figure 5. (**a**) The MB photo-Fenton degradation efficiency of various catalysts under visible irradiation for 60 min; (**b**) photo-Fenton degradation kinetics with first-order linearity of $\ln(C_0/C_t) = kt$ with different catalysts.

With a low concentration of MB, the degradation followed the pseudo-first-order kinetics and the reaction constant of photodegradation was determined by the following equation [28]:

$$\ln(C_0/C_t) = kt$$

where C_0 is the initial dye concentration which reached adsorption–desorption equilibrium in the dark, C_t is the dye concentration at given time t during the Fenton process, and k is

the reaction rate constant. As shown in Figure 5b, the plots $\ln(C_0/Ct)$ versus irradiation time are almost linear, which indicates that the photocatalytic degradation of MB solution agrees with the pseudo-first-order kinetic model. The optimal reaction rate constant was obtained for the 0.07-SnO_2/α-Fe_2O_3 sample (0.0537 min^{-1}), which was more than 2.8 times higher than that of α-Fe_2O_3 (0.0191 min^{-1}). Thus, it can be concluded that SnO_2 shows positive effects on the MB Fenton degradation of α-Fe_2O_3 [46–48]. Previous studies have reported that H_2O_2 could capture the photo-generated electrons of a semiconductor and decompose itself into ·OH for the dye's degradation [49,50]. In this study, all the degradation efficiencies are enhanced with the assistance of H_2O_2 and the degradation efficiency of α-Fe_2O_3 is much higher than that of SnO_2. These might be ascribed to the photo-Fenton reaction of Fe^{2+} and H_2O_2.

To assess the contribution of reactive radicals and further explore catalytic mechanisms, control experiments were carried out with or without scavengers over the 0.07-SnO_2/α-Fe_2O_3 catalyst shown in Figure 6. Isopropanol (IPA) and 1, 4-benzoquinone (BQ) were used as hydroxyl radicals (·OH) and superoxide radical (·O_2) scavengers, respectively. As shown in Figure 6, the catalytic degradation of MB was limited by scavengers. This indicates that both the ·O_2 and ·OH have significant effects on the MB degradation of SnO_2/α-Fe_2O_3.
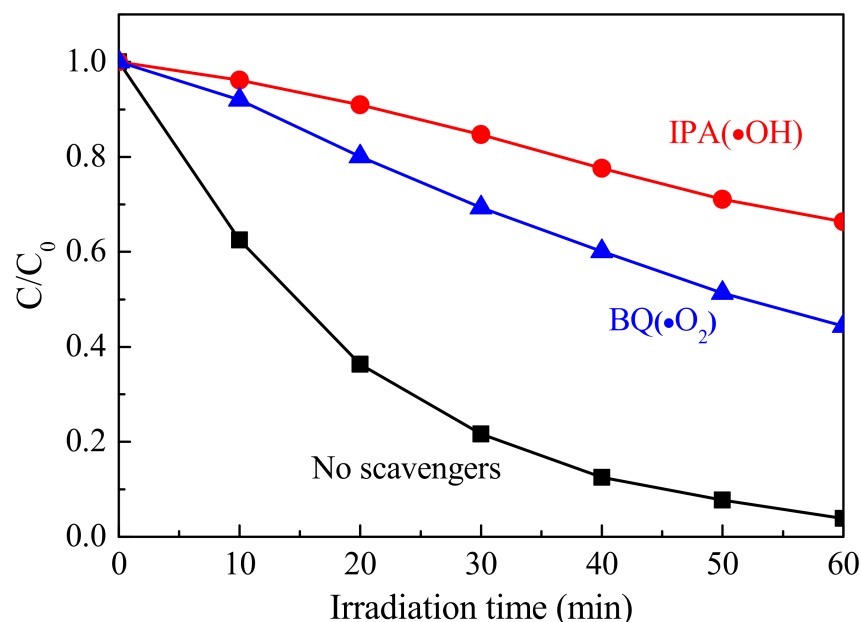

Figure 6. Photo-Fenton degradation of MB with 0.07-SnO_2/α-Fe_2O_3 with and without scavengers.

In addition, experiments on the amount of ·OH generation under α-Fe_2O_3 and 0.07-SnO_2/α-Fe_2O_3 were performed to further explore the effect of SnO_2 on the photo-Fenton reaction. The amount of ·OH in the heterogeneous photo-Fenton reaction was measured based on the fluorescence intensity of hydroxy terephthalic acid. As shown in Figure 7, the concentration of ·OH obviously increases after the introduction of SnO_2, suggesting that the presence of SnO_2 could accelerate the generation of ·OH. This is consistent with the results of the Fenton activity test.

It has been reported that Fe^{3+} could act as an acceptor of photo-generated electrons from a semiconductor during the photocatalytic process to suppress electron–hole recombination [26,28,51,52]. The E_{CB} of SnO_2 (0.4 eV) is more positive than the Fe^{3+}/Fe^{2+} (0.77 eV) redox potential. Therefore, the photoelectrons from CB of SnO_2 could transfer to the Fe^{3+} that are located at the abundant heterogeneous interfaces, and reduce Fe^{3+} to Fe^{2+}. The Fe^{2+} could further react with H_2O_2 and produce more ·OH.
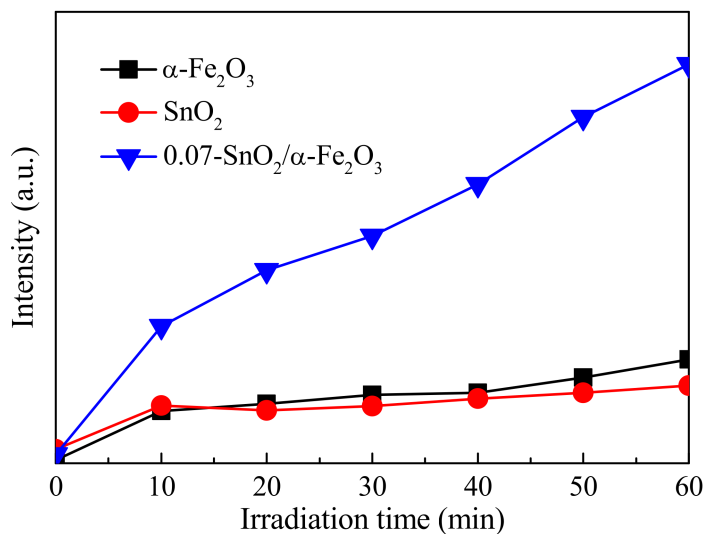
Figure 7. Fluorescence intensity versus time for hydroxy terephthalic acid under different catalysts.

According to the above results, the catalytic mechanism was illustrated in Figure 8. Under visible light irradiation, the photoelectrons (e^-) of the α-Fe_2O_3 are excited, and transition into the conduction band (CB), leaving the same amount of holes (h^+) in the valence band (VB) [40]. The h^+ and e^- can react with H_2O_2 to generate $\cdot O_2$ and $\cdot OH$. The separation of h^+ and e^- can be promoted owing to the presence of numerous H_2O_2 and Fe^{3+}. Meanwhile, the generation of $\cdot O_2$ and $\cdot OH$ can also be accelerated [49,50]. Importantly, the CB of SnO_2 could act as a sink for the generated electrons from the α-Fe_2O_3 and the excited MB molecules. Since the CB position of SnO_2 is more negative than the Fe^{3+} redox potential, these electrons would be captured by the Fe^{3+} on the abundant interface of the SnO_2/α-Fe_2O_3 heterogeneous catalyst, which can accelerate the cycle of Fe^{3+}/Fe^{2+} and the photo-Fenton reaction for the generation of $\cdot OH$ [51–53]. In this way, more $\cdot OH$ and $\cdot O_2$ radicals can be produced in SnO_2/α-Fe_2O_3 compared with the α-Fe_2O_3, resulting in the significant enhancement of photocatalytic properties.
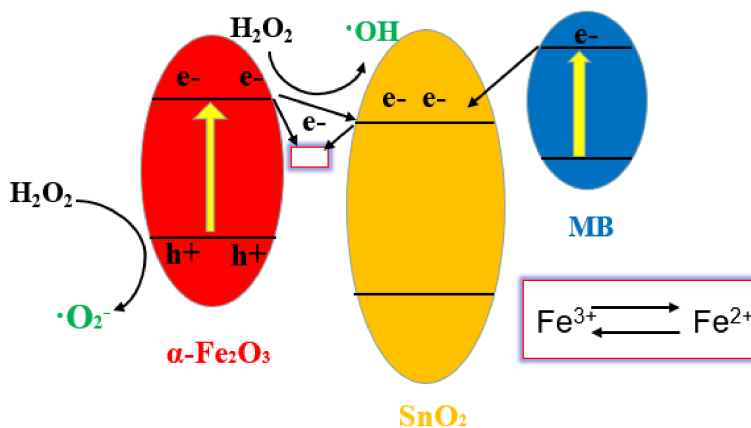

Figure 8. The mechanism for the photo-Fenton degradation of MB with SnO_2/α-Fe_2O_3 under visible light irradiation.

4. Conclusions

In summary, the x-SnO_2/α-Fe_2O_3(x = 0.04, 0.07, and 0.1) heterogeneous catalysts were successfully prepared using a straightforward two-step hydrothermal strategy. The MB photodegradation investigation showed that the SnO_2/α-Fe_2O_3 composites exhibited an excellent photodegradation ability, with the addition of H_2O_2. The rate constant of 0.07-SnO_2/α-Fe_2O_3 composite (0.0537 min^{-1}) is 2.8 times higher than that of pure α-Fe_2O_3

powder (0.0191 min^{-1}). This remarkable enhancement is attributed to the effective transfer of photo-generated electrons for decomposing hydrogen peroxide into active radicals. The catalytic mechanism of the SnO_2/α-Fe_2O_3 heterogeneous catalyst can provide a new insight into the catalytic mechanism of the photo-Fenton process.

Author Contributions: Conceptualization, P.L., X.Z. (Xianmin Zhang) and J.L.; methodology, P.L. and J.L.; validation, Y.J. and X.Z. (Xuye Zhuang); formal analysis, J.X. and Y.J.; resources, X.Z. (Xuye Zhuang) and X.Z. (Xianmin Zhang); data curation, P.L., X.Z. (Xianmin Zhang) and J.L.; writing—original draft preparation, P.L. and Y.J.; writing—review and editing, X.Z. (Xianmin Zhang) and L.R.; supervision, X.Z. (Xuye Zhuang); project administration, L.R. and J.X.; funding acquisition, X.Z. (Xuye Zhuang) and X.Z. (Xianmin Zhang). All authors have read and agreed to the published version of the manuscript.

Institutional Review Board Statement: Not applicable.

Informed Consent Statement: Not applicable.

Data Availability Statement: The data underlying this article will be shared on reasonable request from the corresponding author.

Conflicts of Interest: The authors declare no conflict of interest.

References

1. Zhang, J.; Yan, M.; Sun, G.; Li, X.; Liu, K. Visible-light photo-Fenton catalytic MgFe$_2$O$_4$ spinel: Reaction sintering synthesis and DFT study. *J. Alloy. Compd.* **2021**, *889*, 161673. [CrossRef]
2. Chen, Q.; Ji, F.; Liu, T.; Yan, P.; Guan, W.; Xu, X. Synergistic effect of bifunctional Co–TiO$_2$ catalyst on degradation of Rhodamine B: Fenton-photo hybrid process. *Chem. Eng. J.* **2013**, *229*, 57–65. [CrossRef]
3. Šutka, A.; Šutka, A.; Vanags, M.; Spule, A.; Eglītis, R.; Vihodceva, S.; Šmits, K.; Tamm, A.; Mežule, L. Identifying Iron-Bearing Nanoparticle Precursor for Thermal Transformation into the Highly Active Hematite Photo-Fenton Catalyst. *Catalysts* **2020**, *10*, 778. [CrossRef]
4. Choi, Y.I.; Jung, H.J.; Shin, W.G.; Sohn, Y. Band gap-engineered ZnO and Ag/ZnO by ball-milling method and their photocatalytic and Fenton-like photocatalytic activities. *Appl. Surf. Sci.* **2015**, *356*, 615–625. [CrossRef]
5. Guo, X.; Wang, K.; Li, D.; Qin, J. Heterogeneous photo-Fenton processes using graphite carbon coating hollow CuFe$_2$O$_4$ spheres for the degradation of methylene blue. *Appl. Surf. Sci.* **2017**, *420*, 792–801. [CrossRef]
6. Herney-Ramirez, J.; Vicente, M.A.; Madeira, L.M. Heterogeneous photo-Fenton oxidation with pillared clay-based catalysts for wastewater treatment: A review. *Appl. Catal. B Environ.* **2010**, *98*, 10–26. [CrossRef]
7. Meng, Q.; Wang, K.; Tang, Y.; Zhao, K.; Zhang, G.; Zhao, L. One-pot synthesis of Fe$_2$O$_3$ loaded SiO$_2$ hollow particles as effective visible light photo-Fenton catalyst. *J. Alloy. Compd.* **2017**, *722*, 8–16. [CrossRef]
8. Li, X.; Pi, Y.; Wu, L.; Xia, Q.; Wu, J.; Li, Z.; Xiao, J. Facilitation of the visible light-induced Fenton-like excitation of H$_2$O$_2$ via heterojunction of g-C3N4/NH2-Iron terephthalate metal-organic framework for MB degradation. *Appl. Catal. B Environ.* **2017**, *202*, 653–663. [CrossRef]
9. Guo, L.; Chen, F.; Fan, X.; Cai, W.; Zhang, J. S-doped α-Fe$_2$O$_3$ as a highly active heterogeneous Fenton-like catalyst towards the degradation of acid orange 7 and phenol. *Appl. Catal. B Environ.* **2010**, *96*, 162–168. [CrossRef]
10. Wang, T.; Ge, T.; Zhang, Y. Effects of precursors on the phase, magnetic and photocatalytic properties of nano Fe$_2$O$_3$ synthesized by low temperature calcination. *Colloids Interface Sci. Commun.* **2021**, *44*, 100504. [CrossRef]
11. Liang, H.; Chen, W.; Jiang, X.; Xu, X.; Xu, B.; Wang, Z. Synthesis of 2D hollow hematite microplatelets with tuneable porosity and their comparative photocatalytic activities. *J. Mater. Chem. A* **2014**, *2*, 4340–4346. [CrossRef]
12. Liu, Y.; Yu, C.; Dai, W.; Gao, X.; Qian, H.; Hu, Y.; Hu, X. One-pot solvothermal synthesis of multi-shelled α-Fe$_2$O$_3$ hollow spheres with enhanced visible-light photocatalytic activity. *J. Alloy. Compd.* **2013**, *551*, 440–443. [CrossRef]
13. Zhou, L.; Lei, J.; Wang, L.; Liu, Y.; Zhang, J. Highly efficient photo-Fenton degradation of methyl orange facilitated by slow light effect and hierarchical porous structure of Fe$_2$O$_3$-SiO$_2$ photonic crystals. *Appl. Catal. B Environ.* **2018**, *237*, 1160–1167. [CrossRef]
14. Panda, N.; Sahoo, H.; Mohapatra, S. Decolourization of Methyl Orange using Fenton-like mesoporous Fe$_2$O$_3$–SiO$_2$ composite. *J. Hazard. Mater.* **2011**, *185*, 359–365. [CrossRef]
15. Zhang, G.-Y.; Feng, Y.; Xu, Y.-Y.; Gao, D.-Z.; Sun, Y.-Q. Controlled synthesis of mesoporous α-Fe$_2$O$_3$ nanorods and visible light photocatalytic property. *Mater. Res. Bull.* **2012**, *47*, 625–630. [CrossRef]

16. Wang, C.; Shi, J.; Cui, X.; Wang, H.; Wu, J.; Zhang, C.; Wang, L.; Lv, B.; Xu, Y. Nonspherical hollow α-Fe$_2$O$_3$ structures synthesized by stepwise effect of fluoride and phosphate anions. *J. Mater. Chem. A* **2016**, *4*, 11000–11008. [CrossRef]

17. Zhao, Y.; Pan, F.; Li, H.; Niu, T.; Xu, G.; Chen, W. Facile synthesis of uniform α-Fe$_2$O$_3$ crystals and their facet-dependent catalytic performance in the photo-Fenton reaction. *J. Mater. Chem. A* **2013**, *1*, 7242–7246. [CrossRef]

18. Chan, J.Y.T.; Ang, S.Y.; Ye, E.Y.; Sullivan, M.; Zhang, J.; Lin, M. Heterogeneous photo-Fenton reaction on hematite (α-Fe$_2$O$_3$){104}, {113} and {001} surface facets. *Phys. Chem. Chem. Phys.* **2015**, *17*, 25333–25341. [CrossRef]

19. Wu, W.; Hao, R.; Liu, F.; Su, X.; Hou, Y. Single-crystalline α-Fe$_2$O$_3$ nanostructures: Controlled synthesis and high-index plane-enhanced photodegradation by visible light. *J. Mater. Chem. A* **2013**, *1*, 6888–6894. [CrossRef]

20. Ouyang, J.; Pei, J.; Kuang, Q.; Xie, Z.; Zheng, L. Supersaturation-Controlled Shape Evolution of α-Fe$_2$O$_3$ Nanocrystals and Their Facet-Dependent Catalytic and Sensing Properties. *ACS Appl. Mater. Interfaces* **2014**, *6*, 12505–12514. [CrossRef]

21. Zhou, L.; Wang, L.; Zhang, J.; Lei, J.; Liu, Y. Well-Dispersed Fe$_2$O$_3$ Nanoparticles on g-C$_3$N$_4$ for Efficient and Stable Photo-Fenton Photocatalysis under Visible-Light Irradiation. *Eur. J. Inorg. Chem.* **2016**, *2016*, 5387–5392. [CrossRef]

22. Cui, Z.-M.; Chen, Z.; Cao, C.-Y.; Jiang, L.; Song, W.-G. A yolk–shell structured Fe$_2$O$_3$@mesoporous SiO$_2$ nanoreactor for enhanced activity as a Fenton catalyst in total oxidation of dyes. *Chem. Commun.* **2013**, *49*, 2332–2334. [CrossRef] [PubMed]

23. Uma, K.; Arjun, N.; Pan, G.-T.; Yang, T.C.-K. The photodeposition of surface plasmon Ag metal on SiO$_2$@α-Fe$_2$O$_3$ nanocomposites sphere for enhancement of the photo-Fenton behavior. *Appl. Surf. Sci.* **2017**, *425*, 377–383. [CrossRef]

24. Ursachi, I.; Stancu, A.; Vasile, A. Magnetic α-Fe$_2$O$_3$/MCM-41 nanocomposites: Preparation, characterization, and catalytic activity for methylene blue degradation. *J. Colloid Interface Sci.* **2012**, *377*, 184–190. [CrossRef] [PubMed]

25. Chen, Z.; Liang, Y.; Hao, J.; Cui, Z.-M. Noncontact Synergistic Effect between Au Nanoparticles and the Fe$_2$O$_3$ Spindle inside a Mesoporous Silica Shell as Studied by the Fenton-like Reaction. *Langmuir* **2016**, *32*, 12774–12780. [CrossRef]

26. Zhang, K.; Liu, Y.; Deng, J.; Xie, S.; Lin, H.; Zhao, X.; Yang, J.; Han, Z.; Dai, H. Fe$_2$O$_3$/3DOM BiVO$_4$: High-performance photocatalysts for the visible light-driven degradation of 4-nitrophenol. *Appl. Catal. B Environ.* **2017**, *202*, 569–579. [CrossRef]

27. Liu, Y.; Jin, W.; Zhao, Y.; Zhang, G.; Zhang, W. Enhanced catalytic degradation of methylene blue by α-Fe$_2$O$_3$/graphene oxide via heterogeneous photo-Fenton reactions. *Appl. Catal. B Environ.* **2017**, *206*, 642–652. [CrossRef]

28. Deng, Y.; Xing, M.; Zhang, J. An advanced TiO$_2$/Fe$_2$TiO$_5$/Fe$_2$O$_3$ triple-heterojunction with enhanced and stable visible-light-driven fenton reaction for the removal of organic pollutants. *Appl. Catal. B Environ.* **2017**, *211*, 157–166. [CrossRef]

29. Wang, C.; Du, G.; Ståhl, K.; Huang, H.; Zhong, Y.; Jiang, J.Z. Ultrathin SnO$_2$ Nanosheets: Oriented Attachment Mechanism, Nonstoichiometric Defects, and Enhanced Lithium-Ion Battery Performances. *J. Phys. Chem. C* **2012**, *116*, 4000–4011. [CrossRef]

30. Zhu, S.; Liu, J.; Sun, J. Growth of ultrathin SnO$_2$ on carbon nanotubes by atomic layer deposition and their application in lithium ion battery anodes. *Appl. Surf. Sci.* **2019**, *484*, 600–609. [CrossRef]

31. Zhou, W.; Cheng, C.; Liu, J.; Tay, Y.Y.; Jiang, J.; Jia, X.; Zhang, J.; Gong, H.; Hng, H.H.; Yu, T.; et al. Epitaxial Growth of Branched α-Fe$_2$O$_3$/SnO$_2$ Nano-Heterostructures with Improved Lithium-Ion Battery Performance. *Adv. Funct. Mater.* **2011**, *21*, 2439–2445. [CrossRef]

32. Kim, Y.E.; Baek, U.C.; Kim, J.H.; Chi, W.S.; Park, J.T. Harnessing SnO$_2$ nanotube light scattering cluster to improve energy conversion efficiency assisted by high reflectance. *Mater. Chem. Phys.* **2020**, *254*, 123538. [CrossRef]

33. Zhang, X.; Rui, Y.; Yang, J.; Wang, L.; Wang, Y.; Xu, J. Monodispersed SnO$_2$ microspheres aggregated by tunable building units as effective photoelectrodes in solar cells. *Appl. Surf. Sci.* **2019**, *463*, 679–685. [CrossRef]

34. Zhang, J.; Lou, Y.; Liu, M.; Zhou, H.; Zhao, Y.; Wang, Z.; Shi, L.; Li, D.; Yuan, S. High-Performance Dye-Sensitized Solar Cells Based on Colloid–Solution Deposition Planarized Fluorine-Doped Tin Oxide Substrates. *ACS Appl. Mater. Interfaces* **2018**, *10*, 15697–15703. [CrossRef]

35. Choi, P.G.; Izu, N.; Shirahata, N.; Masuda, Y. Improvement of sensing properties for SnO$_2$ gas sensor by tuning of exposed crystal face. *Sens. Actuators B Chem.* **2019**, *296*, 126655. [CrossRef]

36. Jayababu, N.; Poloju, M.; Reddy, M.R. Facile synthesis of SnO$_2$-Fe$_2$O$_3$ core-shell nanostructures and their 2-methoxyethanol gas sensing characteristics. *J. Alloy. Compd.* **2019**, *780*, 523–533. [CrossRef]

37. Wang, Q.; Kou, X.; Liu, C.; Zhao, L.; Lin, T.; Liu, F.; Yang, X.; Lin, J.; Lu, G. Hydrothermal synthesis of hierarchical CoO/SnO$_2$ nanostructures for ethanol gas sensor. *J. Colloid Interface Sci.* **2018**, *513*, 760–766. [CrossRef]

38. Wang, N.; Du, Y.; Ma, W.; Xu, P.; Han, X. Rational design and synthesis of SnO$_2$-encapsulated α-Fe$_2$O$_3$ nanocubes as a robust and stable photo-Fenton catalyst. *Appl. Catal. B Environ.* **2017**, *210*, 23–33. [CrossRef]

39. Tian, Q.; Wu, W.; Sun, L.; Yang, S.; Lei, M.; Zhou, J.; Liu, Y.; Xiao, X.; Ren, F.; Jiang, C.; et al. Tube-Like Ternary α-Fe$_2$O$_3$@SnO$_2$@Cu$_2$O Sandwich Heterostructures: Synthesis and Enhanced Photocatalytic Properties. *ACS Appl. Mater. Interfaces* **2014**, *6*, 13088–13097. [CrossRef]

40. Niu, M.; Huang, F.; Cui, L.; Huang, P.; Yu, Y.; Wang, Y. Hydrothermal Synthesis, Structural Characteristics, and Enhanced Photocatalysis of SnO$_2$/α-Fe$_2$O$_3$ Semiconductor Nanoheterostructures. *ACS Nano* **2010**, *4*, 681–688. [CrossRef]

41. Devi, L.G.; Shyamala, R. Photocatalytic activity of SnO$_2$−α-Fe$_2$O$_3$ composite mixtures: Exploration of number of active sites, turnover number and turnover frequency. *Mater. Chem. Front.* **2018**, *2*, 796–806. [CrossRef]

42. Kang, J.; Kuang, Q.; Xie, Z.-X.; Zheng, L.-S. Fabrication of the SnO$_2$/α-Fe$_2$O$_3$ Hierarchical Heterostructure and Its Enhanced Photocatalytic Property. *J. Phys. Chem. C* **2011**, *115*, 7874–7879. [CrossRef]

43. Fakhimi, O.; Najafi, A.; Khalaj, G. A facile rout to obtain Al$_2$O$_3$ nanopowder via recycling aluminum cans by sol-gel method. *Mater. Res. Express* **2020**, *7*, 045008. [CrossRef]

44. Ai, X.; Lin, J.; Chang, Y.; Zhou, L.; Zhang, X.; Qin, G. Phase modification of copper phthalocyanine semiconductor by converting powder to thin film. *Appl. Surf. Sci.* **2018**, *428*, 788–792. [CrossRef]

45. Zhang, S.; Li, J.; Niu, H.; Xu, W.; Xu, J.; Hu, W.; Wang, X. Visible-Light Photocatalytic Degradation of Methylene Blue Using SnO_2/α-Fe_2O_3Hierarchical Nanoheterostructures. *ChemPlusChem* **2013**, *78*, 192–199. [CrossRef]

46. Xu, L.; Steinmiller, E.M.P.; Skrabalak, S.E. Achieving Synergy with a Potential Photocatalytic Z-Scheme: Synthesis and Evaluation of Nitrogen-Doped TiO_2/SnO_2 Composites. *J. Phys. Chem. C* **2011**, *116*, 871–877. [CrossRef]

47. Lin, B.; Xu, B.; Zhou, Y.; Zhu, B.; Chen, Y.; Gao, B. Heterostructured SnO_2-pillared Co-doped tantalotungstate with high photocatalytic activity under visible-light irradiation. *Mater. Chem. Phys.* **2013**, *142*, 651–658. [CrossRef]

48. Peng, L.; Zheng, R.-R.; Feng, D.-W.; Yu, H.; Dong, X.-T. Synthesis of eco-friendly porous g-C3N4/SiO_2/SnO_2 composite with excellent visible-light responsive photocatalysis. *Arab. J. Chem.* **2020**, *13*, 4275–4285. [CrossRef]

49. Liu, J.; Wang, B.; Li, Z.; Wu, Z.; Zhu, K.; Zhuang, J.; Xi, Q.; Hou, Y.; Chen, J.; Cong, M.; et al. Photo-Fenton reaction and H_2O_2 enhanced photocatalytic activity of α-Fe_2O_3 nanoparticles obtained by a simple decomposition route. *J. Alloy. Compd.* **2019**, *771*, 398–405. [CrossRef]

50. Ma, Y.; Wang, Q.; Xing, S. Insight into the catalytic mechanism of γ-Fe_2O_3/$ZnFe_2O_4$ for hydrogen peroxide activation under visible light. *J. Colloid Interface Sci.* **2018**, *529*, 247–254. [CrossRef]

51. Pan, S.; Wang, S.; Zhang, Y.; Xu, S.; Kong, F.; Luo, Y.; Tian, Y.; Teng, X.; Li, G. Surface Fe3+-decorated pristine SnO_2 nanoparticles with enhanced ·OH radical generation performance. *Catal. Commun.* **2012**, *24*, 96–99. [CrossRef]

52. Yu, H.; Irie, H.; Shimodaira, Y.; Hosogi, Y.; Kuroda, Y.; Miyauchi, M.; Hashimoto, K. An Efficient Visible-Light-Sensitive Fe(III)-Grafted TiO_2 Photocatalyst. *J. Phys. Chem. C* **2010**, *114*, 16481–16487. [CrossRef]

53. Wu, Q.; Yang, H.; Kang, L.; Gao, Z.; Ren, F. Fe-based metal-organic frameworks as Fenton-like catalysts for highly efficient degradation of tetracycline hydrochloride over a wide pH range: Acceleration of Fe(II)/Fe(III) cycle under visible light irradiation. *Appl. Catal. B Environ.* **2020**, *263*, 118282. [CrossRef]